



Acoustic instability in aerosols

Avshalom Offner · Guy Z. Ramon

Received: 15 September 2020 / Accepted: 12 June 2021
© The Author(s), under exclusive licence to Springer Nature B.V. 2021

Abstract Imposing a temperature gradient on a narrow channel can trigger an acoustic instability, driving self-sustained oscillations of the fluid. The temperature gradient required to trigger the instability is dramatically decreased when the channel wall is covered by a thin film of volatile liquid that can undergo phase change. In the present work, we consider a volatile-droplet aerosol on which a temperature gradient is imposed, and theoretically examine whether the heat and mass transfer between the droplets and gas can trigger the acoustic instability. The aerosol structure is separated into two disparate scales: the droplet ensemble, modelled as a periodic grid of channels through which the gas flows, and the ‘micro-scale’, in which the flow around a single droplet serves as an elementary unit in the periodic structure. This scale separation led to the derivation of a new function that accounts for losses caused by viscous, thermal and diffusive relaxation processes due to droplet–gas interactions. A stability analysis is then performed, utilising the derived ‘loss’ function, calculating the minimum temperature difference, ΔT , that triggers the instability. Our analysis suggests that a non-uniform temperature distribution across aerosols may lead to an acoustic instability, which can subsequently enhance coalescence and agglomeration of droplets within an aerosol. Such phenomenon may be utilised to trigger or enhance the operation of thermoacoustic engines, and may possibly occur naturally in atmospheric clouds due to uneven solar irradiation.

Keywords Aerosol · Thermoacoustic instability

1 Introduction

Acoustic oscillations are long known to be spontaneously triggered in a channel along which a temperature gradient is imposed [1–3]. Small displacements of a compressible fluid within the channel are enhanced due to heat transfer from the (hot) channel wall to the fluid as the latter compresses, and from the fluid to the (cold) wall as it expands [4]. Practical examples of this phenomenon include the Pyrophone [5], a musical instrument in which flames are used to

A. Offner · Guy Z. Ramon (✉)

Department of Civil and Environmental Engineering, Technion - Israel Institute of Technology, 32000 Haifa, Israel
e-mail: ramong@technion.ac.il

A. Offner

Present address: School of Mathematics, The University of Edinburgh, James Clerk Maxwell Building, Peter Guthrie Tait Rd, Edinburgh EH9 3FD, UK
e-mail: avshalom.offner@ed.ac.uk

trigger acoustic waves in tubes of varying lengths; undesired excitation of acoustic oscillations inside combustion chambers due to unsteady heat release [6,7]; and, more recently, the concept of a thermoacoustic engine, where intense acoustic waves are intentionally generated and used as mechanical power or converted to electricity [8–11]. In the latter, very large temperature gradients, aligned with the desired wave propagation direction, are required to trigger the instability. However, a gas mixture containing a condensible specie as the working fluid can dramatically lower the temperature gradient [12–15]. In this configuration, most of the heat is delivered to the gas at constant temperature, in the form of latent heat; the condensible fluid undergoes a cycle of evaporation and condensation, drawing and releasing heat to/from the channel wall, respectively. The linear theory of thermoacoustics, first derived by Rott [16], was modified by Raspet et al. [14] to account for the phase-change heat transfer, and later generalised by Offner et al. [17] to account for various mass transfer mechanisms. The latter also conducted a stability analysis in which the theoretical model was validated against experimental results reported by Tsuda and Ueda [15], revealing a good quantitative agreement.

Acoustic instabilities in aerosols have been studied extensively in the context of photoacoustic spectroscopy. This method can determine material properties via irradiation by an electromagnetic pulse that heats the material, resulting in its expansion, which propagates as an acoustic signal picked up by sensitive ultrasonic transducers [18]. In particular, this method has been used to measure light absorption of aerosols, mainly aerosols of black carbon particles [19]. Raspet et al. [20] investigated light absorption in aerosols of volatile droplets, showing how phase change in the droplets consumes a significant share of the radiative heat. The low radiative flux used in photoacoustic spectroscopy uniformly heats the aerosol, generating acoustic signals intense enough to allow for high-accuracy sensing, yet far too weak to induce significant motion of the suspended matter within the aerosol.

Herein, we speculate on the possible excitation of acoustic oscillations in aerosols of volatile droplets, over which a temperature gradient is imposed. This may naturally occur in atmospheric clouds, where uneven heating creates a temperature gradient within an aerosol [21], which may prove sufficiently large so as to trigger the instability. The complex dynamics of the droplets and gas following the instability is beyond the scope of the current work. However, based on previous studies that demonstrated how aerosol-droplet coagulation is enhanced in an acoustic field [22,23], we suggest that the induced oscillatory motion can lead to coalescence and agglomeration of droplets, possibly enhancing precipitation. From an engineering point of view, aerosols may replace the existing narrow-channel solid structures (typically referred to as ‘stacks’) used in thermoacoustic engines as the hub for acoustic power production [24,25], thus decreasing the number of system parts and potentially reducing viscous losses. In the forthcoming analysis, we theoretically investigate the acoustic instability in an aerosol of volatile droplets. Building upon the works of Raspet et al. [14] and Offner et al. [17], we consider the instability as occurring primarily due to mass transfer between the droplets and gas that comprise the aerosol, showing that a low temperature gradient may be sufficient to trigger the instability. However, the configuration considered here—flow within an aerosol of spherical droplets—is far more complex compared to previous studies, and requires the development of a new method with which to model the flow.

The paper is organised as follows: in Sect. 2 we describe the problem under consideration, Sect. 3 is devoted to the derivation of the theoretical model, in Sect. 4 we investigate the new loss function for aerosols, in Sect. 5 we describe the methodology through which the stability analysis is carried out, followed by results and conclusions in Sects. 6 and 7, respectively.

2 Problem formulation

We consider an aerosol composed of a gas and small spherical droplets, on which a unidirectional temperature difference, ΔT (aligned with the coordinate z), is imposed (see Fig. 1a). Setting $z = 0$ as the left end of the aerosol, we have the region $0 \leq z \leq L$ occupied by the aerosol, while the remaining space is a homogeneous gaseous environment, which may be infinite for atmospheric aerosols or finite in case an aerosol is introduced into a resonator.

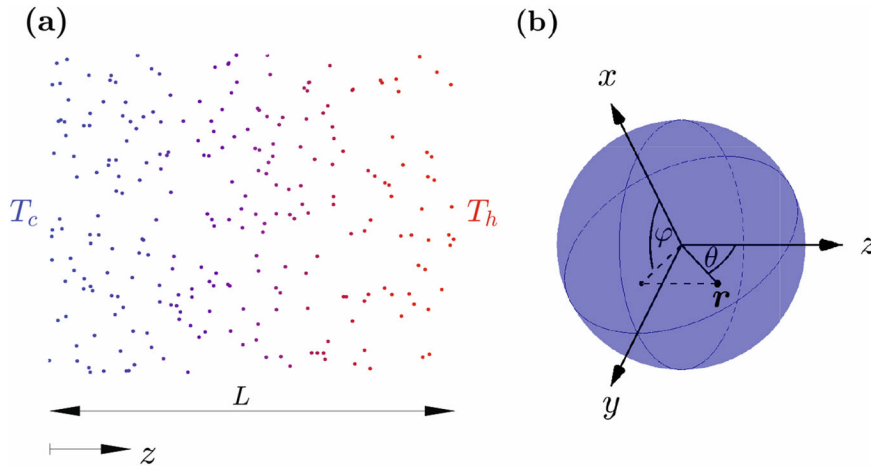


Fig. 1 Schematic drawing of the considered system configuration: **a** an aerosol of length L composed of small droplets with radius R , on which a unidirectional temperature difference, ΔT , is imposed, with T_c and T_h denoting the aerosol cold and hot temperatures, respectively. **b** a close view of a single droplet in the aerosol, showing its system of coordinates in which the local flow field is evaluated. The two images show the problem’s two distinguished scales that are used to recover the flow field in the entire aerosol

The base state of the aerosol is quiescent, where small random pressure fluctuations decay rapidly due to viscous, thermal and diffusive interactions between the droplets and gas [4,26]. Imposing a temperature difference on the aerosol is expected to induce an additional thermoacoustic interaction, in which acoustic power is generated as the gas draws/delivers heat and mass from/to the droplets while oscillating. In case ΔT is sufficiently large, such interaction enhances the oscillations [25]. The stability limit is defined as the state for which the thermoacoustic amplification exactly balances the dissipation, such that further increasing ΔT will lead to a loss of stability in the aerosol.

3 Theoretical model

3.1 Scale separation

Oscillatory flow inside long channels may be described by a linearised axial momentum equation [27],

$$\frac{\partial \bar{v}_z}{\partial \bar{t}} = -\frac{1}{\bar{\rho}_m} \frac{d\bar{p}_1}{d\bar{z}} + \nu \bar{\nabla}_\perp^2 \bar{v}_z, \tag{1}$$

in which the nonlinear terms are omitted on asymptotic grounds, since $h/l \ll 1$ with h and l the channel width and length, respectively. Here, a bar marks a dimensional quantity, t is time, z marks the wave propagation direction, v_z is the fluid velocity component aligned with the oscillations, ρ is the fluid density, p is the pressure, ν is the kinematic viscosity and the ∇_\perp operator denotes derivatives along the axes perpendicular to z . The subscripts ‘ m ’ and ‘1’ denote time-averaged (mean) and oscillating quantities, respectively. Assuming a monochromatic wave resonates in the system, a standard harmonic temporal dependency $\exp(i\omega\bar{t})$ (with ω the resonant frequency) is used for all oscillating variables. Introducing the scaling

$$t = \omega \bar{t}, \quad z = \lambda^{-1} \bar{z}, \quad \nabla_\perp = h \bar{\nabla}_\perp, \quad v_z = \lambda^{-1} \omega^{-1} \bar{v}_z, \quad \rho = \rho_0^{-1} \bar{\rho}, \quad p = \rho_0^{-1} \lambda^{-2} \omega^{-2} \bar{p}, \tag{2}$$

where λ is the wavelength and ρ_0 is the fluid reference density, we rewrite (1) in dimensionless form

$$\left(\nabla_\perp^2 - \hat{\tau}_v^2\right) v_z = \frac{1}{\rho_m} \frac{dp_1}{dz}, \tag{3}$$

where $\tau_v = h(\omega/\nu)^{1/2}$ is the Womersley number and a hat sign denotes multiplication of any scalar quantity by $i^{1/2}$, e.g. $\hat{\tau}_v \equiv i^{1/2}\tau_v$. For a channel of arbitrary cross section, Arnott et al. [28] showed that (3), when subjected to boundary conditions of no-slip at the channel wall and symmetry along its axis, has a general solution of the form

$$v_z = \frac{i}{\rho_m} \frac{dp_1}{dz} H_v, \quad (4)$$

where H_v is a complex viscous ‘loss’ function, unique to the specific channel geometry (e.g. flow inside a circular/square channel or between two parallel plates). For channels of low aspect ratio, it is straightforward to show that both ρ_m and p_1 are a function of z alone [17], such that the velocity profile along the channel cross section is dictated solely by the function H_v .

In what follows, we derive a new loss function for flow past spherical droplets within an aerosol. We consider a sparse aerosol of droplets satisfying $R \ll d$, where R is the droplet radius and d the distance between neighbouring droplets, namely that droplets are very small compared with the distance between them. While the spatial distribution of droplets in an aerosol is generally random, we make the assumption that for $R \ll d$ the flow around any of the droplets is not affected by the presence of neighbouring droplets. Under this assumption the aerosol may be viewed as a periodic structure of droplets, for which the flow field over a single representative droplet may be used to deduce the flow field in the entire ensemble. Following this approach we separate the flow into two disparate scales: the ensemble (macro) scale, in which the aerosol is treated as a set of ‘channels’ through which the gas flows, and the droplet (micro) scale that makes a single elementary unit in the periodic formation. At the ensemble scale the wave propagates through an array of droplets that induce viscous losses, therefore the velocity is assumed to obey (4) with a function H_v derived using the flow field at the single-droplet scale. In the original derivation of (3), ω represents the fundamental (first-mode) resonant frequency of the system. However, here we must distinct between two configurations: in case an aerosol is introduced into a resonator, for example to replace a stack, ω will denote the resonant frequency; if a stand-alone aerosol is considered, the unbounded domain does not allow for resonance conditions to develop, and the solution (4) is employed in the form of a normal mode analysis, where all frequencies can co-exist assuming they do not interact prior to the instability. ΔT then denotes the temperature difference imposed on the aerosol that would trigger the instability for each frequency separately.

The flow field around a single droplet is obtained through a solution to the momentum equations in spherical coordinates (see Fig. 1b for the single-droplet coordinate system). We employ the solution of Lamb [27] to the linearised vorticity equation for flow over an oscillating sphere, in which a no-slip boundary condition on the sphere surface is considered. Internal flow within the sphere—a droplet in our case—can affect the liquid velocity relative to the droplet motion, and thus induce velocity slip at the droplet–gas interface. Considering a tangential-stress balance at the interface, however, suggests that such effect is marginal due to the large dynamic-viscosity ratio between liquid water and air (≈ 50). On this ground, we neglect the internal circulation within the droplet and follow Lamb [27] who derived, through a separation of variables, a solution in terms of the streamfunction

$$\psi(r, \theta, t) = f(r) \sin^2 \theta \exp(it), \quad (5)$$

where

$$f(r) = \frac{1}{2}r^2 - \frac{\mathcal{H}(\hat{\tau}_v)}{2\hat{\tau}_v^2} \frac{1}{r} + \frac{3}{2\hat{\tau}_v} \left(1 + \frac{1}{\hat{\tau}_v r}\right) \exp[\hat{\tau}_v(1-r)] \quad (6)$$

with

$$\mathcal{H}(\xi) := 3 + 3\xi + \xi^2. \quad (7)$$

All quantities are non-dimensional, employing the original scaling of Lamb [27]

$$r = R^{-1}\bar{r}, \quad t = \omega\bar{t}, \quad \psi = \lambda^{-1}\omega^{-1}R^{-2}\bar{\psi}, \quad v = \lambda^{-1}\omega^{-1}\bar{v}, \quad (8)$$

save only the reference velocity U_∞ which is here replaced by $\lambda\omega$. The flow is assumed axisymmetric with respect to $0 \leq \phi \leq 2\pi$ and $\hat{\tau}$ is defined with R as the length scale. The streamfunction is defined such that the incompressible continuity equation is automatically satisfied

$$v_r = \frac{1}{r^2 \sin \theta} \frac{\partial \psi}{\partial \theta}, \quad (9)$$

$$v_\theta = -\frac{1}{r \sin \theta} \frac{\partial \psi}{\partial r}, \quad (10)$$

and the oscillating velocity is, simply,

$$v_z(r, \theta) = \cos \theta v_r - \sin \theta v_\theta. \quad (11)$$

The non-dimensional pressure field may be recovered by considering the time-harmonic, linearised radial momentum equation which, using the scaling introduced in (2), is

$$\frac{\partial p_1}{\partial r} = -\frac{i}{\hat{\tau}_v^2} \frac{R}{\lambda} \rho_m \left[\hat{\tau}_v^2 v_r + \nabla^2 v_r - \frac{2}{r^2} \left(v_r + \frac{\partial v_\theta}{\partial \theta} + v_\theta \cot \theta \right) \right], \quad (12)$$

where

$$\nabla^2 = \frac{1}{r^2} \frac{\partial}{\partial r} \left(r^2 \frac{\partial}{\partial r} \right) + \frac{1}{r^2 \sin \theta} \frac{\partial}{\partial \theta} \left(\sin \theta \frac{\partial}{\partial \theta} \right). \quad (13)$$

In order to derive an expression for the axial pressure derivative we integrate (12) with respect to r using (9) and (10), transform coordinates $r, \theta \rightarrow x, y, z$, take a derivative with respect to z and transform the coordinates back $x, y, z \rightarrow r, \theta$ to finally obtain

$$\frac{\partial p_1}{\partial z} = -\frac{i}{\hat{\tau}_v^2} \rho_m \left[1 - \frac{\mathcal{H}(\hat{\tau}_v)}{2\hat{\tau}_v^2 r^3} (1 - 3 \cos^2 \theta) \right]. \quad (14)$$

Note that the factor R/λ in (12) is eliminated through the (dimensional) integration in $\bar{r} = Rr$ and derivative in $\bar{z} = \lambda z$. Under the assumption that neighbouring droplets do not affect the flow field over a single droplet, we use the expressions in (11) and (14) to rewrite (4) as

$$\begin{aligned} H_v &= -\frac{i \rho_m v_z}{dp_1/dz} \\ &= \frac{4\hat{\tau}_v^2 r^3 - \mathcal{H}(\hat{\tau}_v) (1 + 3 \cos 2\theta)}{4\hat{\tau}_v^2 r^3 + \mathcal{H}(\hat{\tau}_v) (1 + 3 \cos 2\theta)} \left(1 - \exp[\hat{\tau}_v (1 - r)] \frac{4\hat{\tau}_v^2 r^2 - \mathcal{H}(\hat{\tau}_v r) (1 + 3 \cos 2\theta)}{4\hat{\tau}_v^2 r^3 - \mathcal{H}(\hat{\tau}_v) (1 + 3 \cos 2\theta)} \right). \end{aligned} \quad (15)$$

The underlying assumption here is that the ensemble-scale pressure oscillations are a function of z alone, such that any local dependency of the pressure near the droplet on r, θ may be incorporated into the viscous loss function H_v .

A similar process can be applied to the linearised energy and mass conservation equations, deriving H_α and H_D , the loss functions for conductive and diffusive relaxation between the droplets and gas. These functions are expected to recover a result identical to (15), with changes reflected through the appropriate transport coefficient (the subscripts α and D for thermal and mass diffusion, respectively). Consequently, we follow Swift and Keolian [29] who derived a loss function for flow through a pin array of solid material, in which only the viscous loss function was derived explicitly and its form was directly applied for the thermal relaxation loss function H_α , and apply the form of (15) to the respective loss functions H_α and H_D .

3.2 Wave equation and spatial averaging

One-dimensional models for wave propagation are typically employed to describe acoustic instability inside narrow channels of different geometries. The thermoacoustic instability, however, is driven by the interaction between the oscillating gas and the channel wall, through heat and mass transfer perpendicular to the wave propagation direction, and hence the equations are inherently two (or three) dimensional. Retaining a one-dimensional model is achieved through spatial averaging over the channel cross section to obtain an ordinary differential equation (ODE) for the

pressure oscillations in the channel, commonly referred to as the acoustic wave equation. Offner et al. [17] derived such a wave equation for a binary gas mixture containing one ‘reactive’ component that exchanges mass with the boundary, thus incorporating mass transfer as the main mechanism for triggering the instability. For the simple case of mass transfer through evaporation/condensation this dimensionless equation, using the scaling in (2), reads

$$-\frac{d}{dz} \left(\frac{1}{\Phi_u} \frac{dp_1}{dz} \right) + \Phi_T \frac{dp_1}{dz} + \Phi_p p_1 = 0, \tag{16}$$

with

$$\Phi_u = -\frac{i\rho_m}{F_v}, \tag{17}$$

$$\Phi_p = -\frac{i}{p_m} \left[1 - \frac{\gamma - 1}{\gamma} F_\alpha + \frac{C_m}{1 - C_m} (1 - F_D) \right], \tag{18}$$

$$\Phi_T = -\frac{i}{\rho_m} \left[\frac{F_\alpha - F_v}{1 - Pr} \frac{1}{T_m} \frac{dT_m}{dz} + \frac{F_D - F_v}{1 - Sc} \frac{1}{1 - C_m} \frac{dC_m}{dz} \right], \tag{19}$$

where C is the concentration of the volatile component in the gas mixture, in terms of the molar fraction, and

$$F_n(\hat{\tau}_n) = \frac{1}{A} \int H_n dA, \quad n = v, \alpha, D, \tag{20}$$

with A denoting the cross-sectional area of the channel. The functions in (20) represent spatially-averaged losses across the channel cross section, and are the only quantities in (16) that hold information on the channel geometry.

In the current analysis, an aerosol is modelled as a set of channels for which the loss function (15) was derived. The heat and mass transfer occurs between the droplets and the surrounding gas. In order to employ (16) for stability analysis calculations, the spatially-averaged loss functions must be derived; the spherical coordinates impose a new definition,

$$F_n(\hat{\tau}_n, \Upsilon) \equiv \frac{1}{V} \int H_n dV = \frac{1}{4\pi/3(\Upsilon^3 - 1)} \int_0^{2\pi} d\phi \int_0^\pi d\theta \int_1^\Upsilon r^2 \sin\theta H_n dr, \tag{21}$$

in which $\Upsilon = R_\infty/R$ marks the ratio between the upper limit of integration and the droplet radius. In practical terms, Υ represents the approximate distance between neighbouring droplets in the aerosol. The integrals in both ϕ and θ in (21) may be evaluated analytically, to obtain

$$\begin{aligned} F(\hat{\tau}, \Upsilon) = & \frac{3}{\Upsilon^3 - 1} \int_1^\Upsilon \left\{ -r^2 \left(1 - \exp[\hat{\tau}(1-r)] \frac{\mathcal{H}(\hat{\tau}r)}{\mathcal{H}(\hat{\tau})} \right) \right. \\ & + \frac{\sqrt{3}\hat{\tau}^2 r^4 \left(2r - \exp[\hat{\tau}(1-r)] \left[1 + r \frac{\mathcal{H}(\hat{\tau}r)}{\mathcal{H}(\hat{\tau})} \right] \right)}{6\sqrt{\mathcal{H}(\hat{\tau})} [2\hat{\tau}^2 r^3 - \mathcal{H}(\hat{\tau})]} \\ & \left. \times \left[\pi - 2 \arctan \left(\frac{\hat{\tau}^2 r^3 - 2\mathcal{H}(\hat{\tau})}{\sqrt{3\mathcal{H}(\hat{\tau})} [2\hat{\tau}^2 r^3 - \mathcal{H}(\hat{\tau})]} \right) \right] \right\} dr, \tag{22} \end{aligned}$$

where the subscript ‘ n ’ is omitted hereinafter, since τ_v, τ_α and τ_D only differ by the constants $Pr, Sc = O(1)$, the Prandtl and Schmidt numbers, respectively.

4 The complex loss function

The new result (22) represents a ‘loss’ function for transport within an aerosol of spherical droplets. Unlike equivalent loss functions for different geometries (flow in a pipe of circular/square cross section, or between two parallel plates), collectively defined in (20) as a function of a single parameter— $\hat{\tau}$ —the present derivation led to a function of two independent parameters, $\hat{\tau}$ and Υ . This arises from the spherical geometry, as the droplet radius R is used to define $\hat{\tau}$ while the integration domain remains independent. *In what follows, we consider the leading mechanisms affecting the droplet motion, which subsequently determine the parameter range for which (22) is valid.*

4.1 Gravity

Droplets suspended in a gas fall under the influence of gravity, at a rate dictated by the balance between their weight and the drag force acting upon them due to their motion. For small droplets, satisfying $Re \ll 1$, where $Re = UR/\nu$ is the *Reynolds* number, Stoke’s drag is invoked to describe the droplet dynamics, leading to a droplet terminal velocity

$$v_t = \frac{2(\vartheta - 1)gR^2}{9\nu}, \quad (23)$$

where g is the gravitational acceleration and $\vartheta = \rho_d/\rho_g$ is the ratio between the droplet and gas densities. For the majority of aerosols, $\vartheta \gg 1$, such that $\vartheta - 1 \approx \vartheta$ may be substituted ($\vartheta \approx 10^3$ for water droplets suspended in atmospheric air). We define a gravitational time scale, $t_g = R/v_t$, as the time over which a droplet covers a distance R . For the acoustic instability to be triggered, a droplet should not undergo substantial displacement in the direction of the temperature gradient, ∇T , during an oscillation cycle. Accordingly, we define a ratio between the oscillation and gravitational time scales,

$$\mathcal{W} = \frac{t_\omega}{t_g / \cos \Theta} = \frac{2\vartheta g R \cos \Theta}{9\nu\omega}, \quad (24)$$

where $0 \leq \Theta \leq \pi/2$ marks the misalignment between the directions of g and ∇T , and we further demand that $\mathcal{W} \ll 1$. For water droplets in air with $\cos \Theta = 1$, we have $\mathcal{W} \approx 10^8 R/\omega \ll 1$, revealing that $R\omega^{-1}$ must be very small in order to allow for oscillations to be spontaneously triggered, given that $\Theta \neq \pi/2$. This condition may be satisfied by considering ultrasonic frequencies ($\omega \gtrsim 10^5 \text{ s}^{-1}$), however, such oscillations are unlikely to affect the aerosol even if triggered, and are therefore of less interest. For lower frequencies, $R\omega^{-1} \ll 1$ is obtained for $\tau \ll 1$, since $\tau \propto R\omega^{1/2}$.

4.2 Droplet entrainment

Equation (22) is derived assuming that the droplet is immobilised, however, droplets can become entrained in the air that surrounds them. To account for this entrainment, we employ the result of Song et al. [30], who derived a simple expression for droplet entrainment,

$$\eta = \frac{1}{1 + \frac{2\vartheta}{9}\hat{\tau}_v^2}, \quad (25)$$

in which $\eta \rightarrow 1$ and $\eta \rightarrow 0$ denote complete and no entrainment, respectively. With entrainment, the gas velocity over a droplet is taken as the gas–droplet relative velocity, and hence a factor $1 - \eta$ multiplies v_z in the original definition (15) leading to the derivation of the loss function, F . Consequently, F is modified so as to incorporate the droplet entrainment, viz.

$$\mathcal{F}(\hat{\tau}, \Upsilon) = E(\hat{\tau}) F(\hat{\tau}, \Upsilon), \quad (26)$$

where

$$E(\hat{\tau}) = \frac{2\vartheta \hat{\tau}^2}{9 + 2\vartheta \hat{\tau}^2}. \tag{27}$$

As expected, smaller droplets are more entrained with the gas, leading to vanishingly small \mathcal{F} for $\tau < 10^{-3}$. Consequently, we constrain our range of interest for τ to moderately small values, for which droplets are not fully entrained with the air all the while not being sorely affected by gravity.

4.3 Analytic approximation

In order to simplify (22), we note that the geometry of flow over a single sphere resembles that of flow over a flat plate, with the added complexity of surface curvature. The loss function for flow over a flat plate is simply $F = 1 - \hat{\tau}^{-1}$ [25], clearly revealing that the function is valid for $\tau \geq O(1)$, since smaller values correspond to narrow channels, where the effect of the opposite plate (in parallel plates geometry) cannot be neglected. To determine an equivalent range for the validity of (22), we define a new non-dimensional number

$$\mathcal{T} = \tau\mathcal{Y} = R_\infty (\omega/n)^{1/2}, \quad n = \nu, \alpha, D. \tag{28}$$

The droplet radius cancels in the multiplication $\tau\mathcal{Y}$, and \mathcal{T} resembles the definition of τ in a long channel, with R_∞ representing the dimensional length scale of the ‘channel’ between neighbouring droplets. It is, then, straightforward to set $\mathcal{T} \geq O(1)$ as the condition for which (22) is valid. Accordingly, we rewrite (26) using (22) and make the substitution of variables $\hat{\zeta} = \hat{\tau}r$, to obtain

$$\begin{aligned} \mathcal{F}(\hat{\tau}, \hat{\mathcal{T}}) &= \frac{3E(\vartheta^{1/2}\hat{\tau})}{\hat{\mathcal{T}}^3 - \hat{\tau}^3} \int_{\hat{\tau}}^{\hat{\mathcal{T}}} \left\{ i\hat{\zeta}^2 \left(1 - \exp[\hat{\tau} - \hat{\zeta}] \frac{\mathcal{H}(\hat{\zeta})}{\mathcal{H}(\hat{\tau})} \right) \right. \\ &\quad \left. + \frac{\sqrt{3}\hat{\zeta}^5 \left(2 - \exp[\hat{\tau} - \hat{\zeta}] \left[\frac{\hat{\tau}}{\hat{\zeta}} + \frac{\mathcal{H}(\hat{\zeta})}{\mathcal{H}(\hat{\tau})} \right] \right)}{6\hat{\tau}^{1/2} \sqrt{\mathcal{H}(\hat{\tau})} [2\hat{\zeta}^3 - \hat{\tau}\mathcal{H}(\hat{\tau})]} \right. \\ &\quad \left. \times \left[\pi - 2 \arctan \left(\frac{\hat{\zeta}^3 - 2\hat{\tau}\mathcal{H}(\hat{\tau})}{\hat{\tau}^{1/2} \sqrt{3\mathcal{H}(\hat{\tau})} [2\hat{\zeta}^3 - \hat{\tau}\mathcal{H}(\hat{\tau})]} \right) \right] \right\} d\hat{\zeta}, \tag{29} \end{aligned}$$

where a hat sign, as before, marks a multiplication by $i^{1/2}$.

Next, we simplify (29) by considering the asymptotic limit $\tau \ll 1$ and expanding the integrand as a series near $\hat{\tau} = 0$. The entrainment factor $E(\vartheta^{1/2}\hat{\tau})$ is deliberately excluded from the expansion since $\vartheta^{1/2} \gg 1$, and the limit $\tau \rightarrow 0$ necessitates that $\mathcal{F} \rightarrow 0$. We then split the integral into two distinct regions: $\hat{\tau} \rightarrow \hat{\sigma}$ and $\hat{\sigma} \rightarrow \hat{\mathcal{T}}$, where $\hat{\sigma}$ marks the lowest value, for which $\hat{\tau} \ll \hat{\zeta}$ in the integrand. Since $\mathcal{T} \geq O(1)$ and $\tau \ll 1$, we concentrate on the case $\tau \ll \sigma \ll 1$, in which the contribution of the region $\hat{\tau} \rightarrow \hat{\sigma}$, where the series expansion in $\hat{\tau}$ is not valid, may be neglected. Setting $\hat{\sigma} = 0$ for simplicity, we have

$$\mathcal{F}(\hat{\tau}, \hat{\mathcal{T}}) = \frac{3E(\vartheta^{1/2}\hat{\tau})}{\hat{\mathcal{T}}^3} \int_0^{\hat{\mathcal{T}}} \left\{ \hat{\zeta}^2 - \hat{\tau}\hat{\zeta} \exp(-\hat{\zeta}) \right\} d\hat{\zeta} + O(\tau^2), \tag{30}$$

which is easily integrated to finally obtain

$$\mathcal{F}(\hat{\tau}, \hat{\mathcal{T}}) = E(\vartheta^{1/2}\hat{\tau}) \left(1 - 3\hat{\tau} \left[\frac{1 - (1 + \hat{\mathcal{T}}) \exp(-\hat{\mathcal{T}})}{\hat{\mathcal{T}}^3} \right] + O(\tau^2) \right). \tag{31}$$

Excluding the entrainment factor, the leading order in (31), $F = 1$, is the result for a lossless channel, to which F physically converges as droplets become smaller and resemble points, i.e. as $\tau (\propto R) \rightarrow 0$. In practice, however, as droplets get smaller they become nearly fully entrained with the air, making a thermoacoustic instability unlikely to be triggered.

Figure 2 displays the real and imaginary components of the aerosol loss function, evaluated both numerically and analytically through (29) and (31), respectively. In Figs. 2a and 2b, we sketched the real and imaginary components of \mathcal{F} as a function of \mathcal{T} for representative values of τ satisfying $\tau \ll 1$. As clearly seen in (31), the $O(\tau)$ correction rapidly vanishes as \mathcal{T} is increased, resulting in $\mathcal{F} \rightarrow E(\hat{\tau})$, providing the values to which the curves saturate at large \mathcal{T} . Physically, this represents a sparse aerosol, for which droplet entrainment alone initiates acoustic attenuation in the fluid surrounding the droplet. As τ is increased, droplets are less entrained and the curves saturate towards $\mathcal{F} \rightarrow 1 + 0i$, representative of all narrow-channel geometries for $\tau \rightarrow \infty$. The analytic approximation (31) closely follows the numerical calculation for $\mathcal{T} \gtrsim 2$. Recalling that the current derivation is valid for $\mathcal{T} \gtrsim O(1)$, (31) may be used to genuinely describe the aerosol loss function throughout much of the range for τ, \mathcal{T} . In Fig. 2c and d, we re-plotted the aerosol curves for $\tau = 0.3$ (blue), alongside curves for other narrow-channel geometries—namely flow over a single plate (red, dashed) and between two parallel plates (red, solid)—sketched against their single parameter, τ . The single plate loss function closely approximates that for parallel plates at large τ , i.e. for widely separated plates. The shaded area marks the range for which the relative error between these functions is less than 5%— $\tau > 2.3$. Recasting this result as the appropriate range for \mathcal{T} in the aerosol loss function proposes a reasonable choice: results below this value drop to negative values (not seen in Fig. 2c, d)—non-physical results marking a flip in the direction of ∇T —while results above it follow the parallel plates curve trend, with the obvious change of saturating to a non-zero constant value due to droplet entrainment. Within this range, the analytic approximation (31) may be used to accurately describe $\mathcal{F}(\tau, \mathcal{T})$ with a relative error not exceeding 6% for $\tau \leq 0.3$.

The methodology applied to derive (29) shares very little in common with the derivation of $F(\tau)$ for different channel geometries, in which the unsteady Stokes equation is explicitly solved [25]. The agreement between the curves' trends in Fig. 2c–d is, then, encouraging and suggests that the use of a single droplet as an elementary unit in a periodic array of droplets results in a loss function for the entire array, which shares features with functions that are regularly used to accurately model physical systems.

5 Stability analysis

In the current analysis, we seek the critical temperature difference, ΔT . The resulting neutral stability curve represents the point where a small pressure perturbation within the aerosol neither decays nor grows. The methodology used to solve for ΔT is thoroughly described in Offner et al. [17], and is therefore only briefly discussed here. Assuming that the gas within the aerosol is saturated with vapour, we use the Clausius–Clapeyron relation to express the reactive gas mole fraction as a function of the gas mixture temperature to obtain

$$C_m = \exp \left[-\frac{l_h}{R_g} \left(\frac{1}{T_m} - \frac{1}{T_b} \right) \right], \quad (32)$$

$$\frac{dC_m}{dz} = \frac{dC_m}{dT_m} \frac{dT_m}{dz} = \frac{l_h}{R_g T_m} \frac{C_m}{T_m} \nabla T, \quad (33)$$

where l_h [J/mol] and T_b are the reactive gas latent heat of vaporisation and boiling temperature, respectively, and R_g is the universal gas constant. For the purpose of the derivation to follow, we rewrite the wave equation (16) as a set of two first-order ODEs

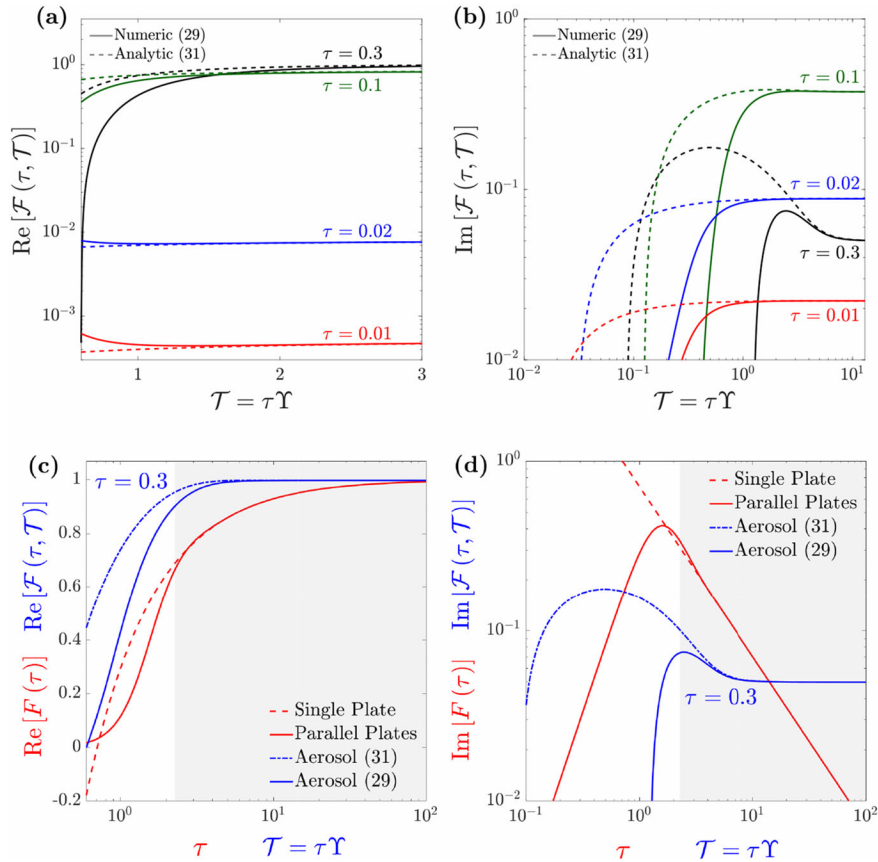


Fig. 2 Real (a) and imaginary (b) components of the complex loss function for oscillating flow within an aerosol, calculated both numerically (solid curves) through (29) as well as analytically (dashed curves) via (31). All curves reach a constant value for large \mathcal{T} , determined by the entrainment factor $E(\hat{\tau}) = 2\vartheta \hat{\tau}^2 / (9 + 2\vartheta \hat{\tau}^2)$. Comparison between the real (c) and imaginary (d) components of the aerosol loss function with $\tau = 0.3$ (blue curves) with that of flow over a single plate (red, dashed curves), sketched against its single parameter, τ . The single plate function closely approximates that of flow between two parallel plates (red, solid curves) for large τ ; the shaded area marks the τ range for which the relative error between these functions is less than 5%— $\tau > 2.3$. Applying this result for the range of \mathcal{T} in the aerosol loss function yields a sensible range, for which the aerosol function closely resembles that of other geometries

$$\frac{dp_1}{dz} = \Phi_u u_1, \tag{34}$$

$$\frac{du_1}{dz} = \Phi_p p_1 + \Phi_T \nabla T u_1, \tag{35}$$

where $u_1 = V^{-1} \int v_z dV$ is the volume-averaged axial velocity, Φ_u, Φ_p are defined in (17–18), respectively, and Φ_T is redefined using (33) to exclude ∇T

$$\Phi_T = -\frac{1}{T_m F_v} \left(\frac{F_\alpha - F_v}{1 - Pr} + \frac{F_D - F_v}{1 - Sc} \frac{C_m}{1 - C_m} \frac{l_h}{R_g T_m} \right). \tag{36}$$

We follow previous work, assuming the axial temperature distribution before an instability is triggered follows a linear trend, i.e. the solution to a one-dimensional, steady conduction equation (see, e.g. [17, 31–33]). The temperature gradient imposed on the aerosol is then simply a constant, $\nabla T = \Delta T/L$, and (34–35) are a set of linear, homogeneous ODEs that form an eigen value problem for the system resonant frequency, ω . We fix the aerosol cold temperature at the left end, $T_m(z = 0) = T_c$, and apply boundary conditions according to the system geometry:

no penetration conditions, i.e. $u_1 = 0$, at closed ends for straight tubes (standing wave resonators); continuation on p_1, u_1 for toroidal tubes (travelling wave resonators). Since the derived aerosol loss function is valid only for $\mathcal{T} \gtrsim \mathcal{O}(1)$, the instability is unlikely to be triggered in travelling wave configurations, for which $\mathcal{T} \ll 1$ is favourable [25]. Consequently, we limit the current analysis to a standing wave configuration, namely a straight tube with closed ends. The temperature is assumed to be constant outside the aerosol (T_c to the left of the aerosol and $T_c + \Delta T$ to the right of it). Newton's method is used to solve the boundary value problem (BVP) and recover ω and ΔT .

6 Results and discussion

We conduct a parametric investigation of the critical temperature difference, ΔT , across an aerosol as a function of several key parameters. The value of $\Delta T \leq \Delta T_{\max} = T_b - T_c$ is bounded, since the aerosol temperature cannot exceed the droplet boiling temperature T_b , nor fall below T_c , which is given as a boundary condition at $z = 0$ [17]. Throughout the forthcoming calculations, we consider a closed, straight tube with diameter 1 cm and length 20 cm, in which an aerosol constitutes a short segment of 1 cm, located 16 cm from the tube's left end. The tube's length, directly affecting the resonant frequency, ω , was chosen such that the condition $\mathcal{W} (\propto R/\omega) \ll 1$ is satisfied (see Sect. 4.1) for realisable droplet radii— $R = 1 - 50 \mu\text{m}$. The aerosol is composed of water droplets suspended in an air–water vapour gas mixture, where the mean pressure is $p_m = 1$ bar.

6.1 Aerosol characteristics

We begin by examining the effect of the aerosol loss function parameters on the critical temperature difference. For convenience, we calculated stability curves for several aerosol sparseness values, \mathcal{Y} , as a function of the aerosol Womersley number, \mathcal{T} , presented in Fig. 3a. All curves display a minimum value, ΔT_{\min} , at unique \mathcal{T} values, where an increase in \mathcal{Y} lowers this minimum until, for $\mathcal{Y} > 30$, ΔT_{\min} remains constant. To explain this phenomenon, we 'artificially' rewrite (31) as a function of three variables (rather than two), to obtain

$$\mathcal{F}(\hat{\tau}, \mathcal{Y}, \hat{\mathcal{T}}) = E(\hat{\tau}) \left(1 - \frac{3}{\hat{\mathcal{T}}} \left[\frac{1 - (1 + \hat{\mathcal{T}}) \exp(-\hat{\mathcal{T}})}{\hat{\mathcal{T}}^2} \right] \right), \quad (37)$$

recalling that $\hat{\mathcal{T}}/\hat{\tau} = \mathcal{Y}$. In this form, it is straightforward how $\mathcal{F} \rightarrow E(\hat{\tau})$ as \mathcal{Y} is increased. At small \mathcal{Y} , Stokes' drag affects the air flow; as the aerosol becomes sparser, this effect diminishes until, for $\mathcal{Y} \gtrsim 50$, it becomes negligible and ΔT_{\min} remains constant. Physically, this implies that an instability is equally likely to be triggered in aerosols of varying sparseness ($\mathcal{Y} > 50$), given that τ is maintained constant. For better illustration, we have redrawn the curves in Fig. 3b as a function of τ alone, showing how these converge to a single curve at large \mathcal{Y} . The τ range for which an instability may be triggered is greatly confined, reflecting the constraints of entrainment, which drastically suppresses the instability at small τ , and that of gravity, which restricts τ to moderately small values for a given ω (see Sects. 4.1 and 4.2 for a detailed explanation).

6.2 Aerosol temperature

The aerosol cold-side temperature $T_c = T_m(z = 0)$ is a prescribed boundary condition that directly affects the reactive gas concentration in the mixture, C_m . This, in turn, strongly affects the phase-change heat transfer between the droplets and gas, tending to decrease ΔT as T_c is increased. Figure 4a presents stability curves at varying T_c for a fixed value of $\mathcal{Y} = 50$ and several representative values of τ . All curves display a monotonically decreasing trend, demonstrating how enriching the vapour content in the gas mixture enhances mass transfer, which translates to a lower ΔT . The minimum value for each curve reflects the results in Fig. 3b, with a minimum value at $\tau \approx 0.17$

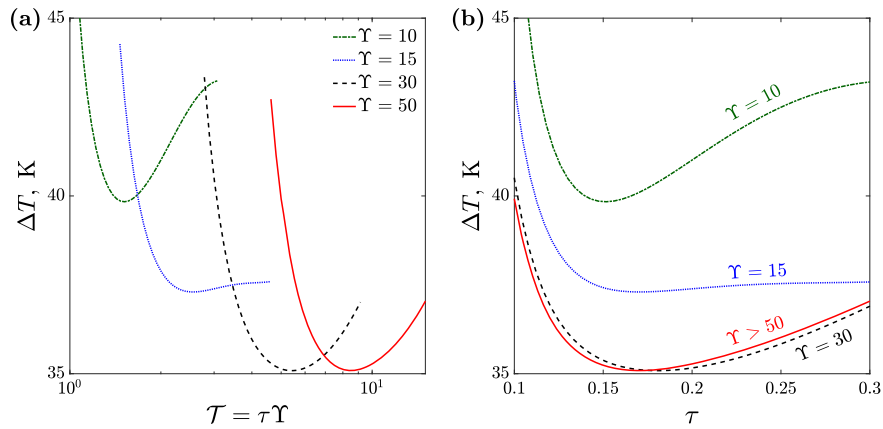


Fig. 3 **a** Critical temperature difference, ΔT , as a function of the aerosol ‘channel’ number, \mathcal{T} , for representative values of aerosol sparseness, Γ . All curves display a minimum at unique \mathcal{T} ; curves for larger Γ (not sketched) recover the $\Gamma = 50$ curve shape, only shifted towards larger \mathcal{T} . The aerosol cold temperature is $T_c = 300$ K. **b** The same stability curves sketched against τ , revealing that large Γ recovers an identical curve, regardless of the aerosol sparseness. The air volume around each droplet at large Γ is large enough to practically eliminate the effect of Stokes drag, leaving only droplet entrainment to attenuate the acoustic wave

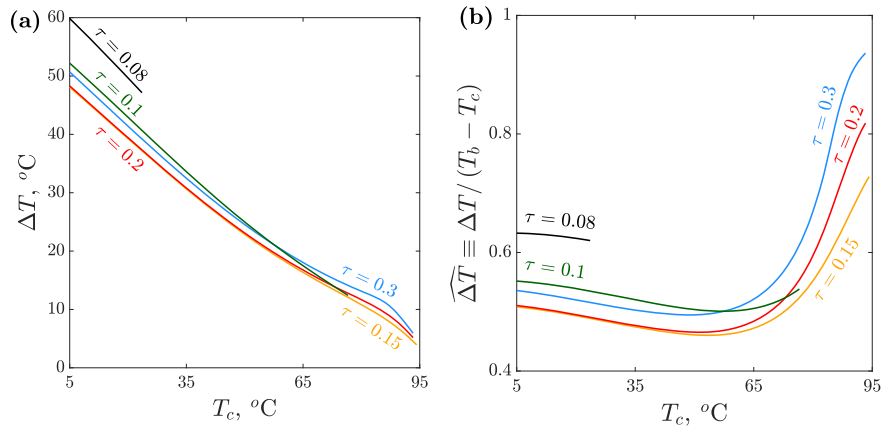


Fig. 4 **a** The temperature difference, ΔT , across an aerosol as a function of the aerosol cold-side temperature, T_c , for fixed $\Gamma = 50$ and several values of τ . All curves decrease monotonically, reflecting a decrease in ΔT as the aerosol temperature increases and mass transfer is enhanced. **b** The scaled temperature difference, $\widehat{\Delta T} \equiv \Delta T / \Delta(T_b - T_c)$, with T_b the reactive gas boiling temperature at mean pressure $p_m = 1$ bar, as a function of T_c . The curves terminate before reaching $\widehat{\Delta T} \rightarrow 1$ due to droplet entrainment, unevenly affecting the instability at varying τ (see Sect. 6.2)

for $\Gamma > 50$. From the previous work [17], the temperature difference is known to drop until $\Delta T \rightarrow \Delta T_{\max}$, where $\Delta T_{\max} \equiv T_b - T_c$ with T_b the boiling temperature, which the reactive gas at a constant mean pressure cannot exceed. Here, however, the $\tau \leq 0.1$ curves terminate well before ΔT approaches ΔT_{\max} . To further investigate this, we scaled the curves by ΔT_{\max} and plotted them in Fig. 4b. At low T_c , an increase in the aerosol temperature dramatically decreases ΔT , outweighing the linear decrease in ΔT_{\max} . As the temperature is further increased, these contributions balance at $T_c \approx 50^\circ\text{C}$, above which the curves ascend and terminate at a finite $\widehat{\Delta T} < 1$. While each curve is labelled with a constant τ , each label corresponds to a mean value since the resonant frequency ω —used to define τ —is the system eigenvalue, unique to each BVP. As T_c is increased, the gas composition changes, tending to increase the sound velocity since water vapour is lighter than air. Consequently, ω increases and so does $\tau \propto \omega^{1/2}$. This variation affects the results through the droplet entrainment factor $E(\hat{\tau}) = 2\vartheta \hat{\tau}^2 / (9 + 2\vartheta \hat{\tau}^2)$. For small τ , the variation in ω dramatically affects the entrainment and therefore the range for which the instability may be triggered, as evident in the $\tau = 0.08, 0.1$ curves that terminate at $T_c = 23, 76^\circ\text{C}$, respectively. At larger τ the

curves all terminate at $T_c \approx 93^\circ\text{C}$, however, the $\widehat{\Delta T}$ value at which they terminate increases with an increase in τ . The variation in ω as T_c increases become less significant, allowing the curves to ascend more towards $\widehat{\Delta T} = 1$.

7 Conclusion

Motivated by the possible implications of acoustic oscillations in aerosols, particularly to the potential enhancement of droplet agglomeration and the use of aerosols to replace existing solid parts in thermoacoustic engines, the present work examined the possible occurrence of acoustic instability in aerosols, triggered by an imposed temperature gradient. Throughout the derivation, the aerosol was modelled as a periodic structure of small, mono-dispersed droplets. The droplets were collectively viewed as a periodic grid of narrow channels, through which the gas flows. The analytic solution to oscillatory flow over a single droplet was then employed to deduce the flow field in the entire ensemble. Applying this methodology, a new function accounting for viscous losses in the aerosol was derived, which was subsequently used to perform a one-dimensional, linear stability analysis identifying the critical temperature difference that triggers the instability. Due to the spherical geometry of the droplets, the derived loss function is dependent on two parameters (as opposed to only one—the *Womersley* number, τ —for other channel geometries), and is expressed as an integral that may only be evaluated numerically. In the limit $\tau \ll 1$, however, the integral may be greatly simplified, allowing the derivation of an analytic solution. The behaviour of this new loss function resembles that of other narrow-channel geometries that are widely used in models of thermoacoustic systems, suggesting that the scale separation technique used in Sect. 3.1 to model the oscillatory flow within the aerosol captures the key physics in this complex flow.

A stability analysis was conducted, in which ΔT was calculated for varying $\mathcal{T} \equiv \tau\gamma$, i.e. the *Womersley* number for the ‘channel’ between neighbouring droplets (see Fig. 3a). The results revealed a self-similar behaviour for sparse aerosols— $\gamma \gtrsim 50$ —where the volume of gas subjected to Stokes’ drag becomes negligible, leaving only the effect of droplet entrainment to attenuate the acoustic wave and induce the instability. Indeed, when plotted against τ (Fig. 3b) all results collapse to a single curve for $\gamma \gtrsim 50$, representing the droplet entrainment dependency on a single parameter, τ .

Effects of the aerosol temperature on the instability were examined by varying the boundary condition for the aerosol cold temperature, T_c . This variation in temperature directly affects the gas mixture composition, expressed as the reactive gas concentration C_m which, in turn, lowers ΔT . While the monotonically decreasing trend of ΔT vs. T_c in Fig. 4a directly matches the results of Offner et al. [17], the curves terminate before reaching their maximal allowed temperature difference, ΔT_{\max} , dictated by the reactive gas boiling temperature. The seemingly small variations in ω due to an increase in T_c prove sufficient to non-negligibly affect droplet entrainment, resulting in suppression of the instability before $\Delta T \rightarrow \Delta T_{\max}$.

The overall results from this work suggest that triggering of acoustic instability in aerosols due to uneven heating may be possible. Once triggered, the excited oscillations induce motion within the aerosol that can subsequently lead to coalescence and agglomeration of droplets.

Acknowledgements The research was funded the Israel Science Foundation (Grant # 2018/17).

Declarations

Conflict of interest The authors declare that they have no conflict of interest.

References

1. Baron Rayleigh JWS (1878) The theory of sound, vol 2. Macmillan and Co, New York
2. Rijke PL (1859) Notiz über eine neue Art, die in einer an beiden Enden offenen Röhre enthaltene Luft in Schwingungen zu versetzen. Ann Phys 183(6):339–343

3. Sondhauss C (1850) Ueber die Schallschwingungen der Luft in erhitzten Glasröhren und in gedeckten Pfeifen von ungleicher Weite. *Ann Phys* 155(1):1–34
4. Swift GW (1988) Thermoacoustic engines. *J Acoust Soc Am* 84(4):1145–1180
5. Dunant JH (1875) The pyrophone. *Popular Sci Month* 7:444–453
6. Keller JJ (1995) Thermoacoustic oscillations in combustion chambers of gas turbines. *AIAA J* 33(12):2280–2287
7. Utvik DH, Ford HJ, Blackman AW (1966) Evaluation of absorption liners for suppression of combustion instability in rocket engines. *J Spacecraft Rockets* 3(7):1039–1045
8. Backhaus S, Swift GW (1999) A thermoacoustic stirling heat engine. *Nature* 399(6734):335–338
9. Bi T, Wu Z, Zhang L, Yu G, Luo E, Dai W (2017) Development of a 5 kW traveling-wave thermoacoustic electric generator. *Appl Energy* 185:1355–1361
10. Yazaki T, Iwata A, Maekawa T, Tominaga A (1998) Traveling wave thermoacoustic engine in a looped tube. *Phys Rev Lett* 81(15):3128–3131
11. Yu Z, Jaworski AJ, Backhaus S (2012) Travelling-wave thermoacoustic electricity generator using an ultra-compliant alternator for utilization of low-grade thermal energy. *Appl Energy* 99:135–145
12. Meir A, Offner A, Ramon GZ (2018) Low-temperature energy conversion using a phase-change acoustic heat engine. *Appl Energy* 231:372–379
13. Noda D, Ueda Y (2013) A thermoacoustic oscillator powered by vaporized water and ethanol. *Am J Phys* 81(2):124–126
14. Raspet R, Slaton WV, Hickey CJ, Hiller RA (2002) Theory of inert gas-condensing vapor thermoacoustics: propagation equations. *J Acoust Soc Am* 112(4):1414–1422
15. Tsuda K, Ueda Y (2017) Critical temperature of traveling- and standing-wave thermoacoustic engines using a wet regenerator. *Appl Energy* 196:62–67
16. Rott N (1969) Damped and thermally driven acoustic oscillations in wide and narrow tubes. *Zeitschrift für angewandte Mathematik und Physik ZAMP* 20(2):230–243
17. Offner A, Yang R, Felman D, Elkayam N, Agnon Y, Ramon GZ (2019) Acoustic oscillations driven by boundary mass exchange. *J Fluid Mech* 866:316–349
18. Rosenzweig A (1990) Photoacoustics and photoacoustic spectroscopy. R.E. Krieger Pub, Co, Oxford
19. Kotzick R, Niessner R (1998) Atmospheric black carbon measurements using photoacoustic spectroscopy. *J Aerosol Sci* 29(Suppl. 1):629–630
20. Raspet R, Slaton WV, Arnott WP, Moosmüller H (2003) Evaporation-condensation effects on resonant photoacoustics of volatile aerosols. *J Atmos Ocean Technol* 20(5):685–695
21. Su J, McCormick MP, Wu Y, Lee RB, Lei L, Liu Z, Leavor KR (2013) Cloud temperature measurement using rotational Raman lidar. *J Quant Spectrosc Radiat Transfer* 125:45–50
22. Foster MP, Pflaum JC (1988) The behavior of cloud droplets in an acoustic field: a numerical investigation. *J Geophys Res* 93(D1):747–758
23. Shaw DT, Tu KW (1979) Acoustic particle agglomeration due to hydrodynamic interaction between monodisperse aerosols. *J Aerosol Sci* 10(3):317–328
24. Hariharan NM, Sivashanmugam P, Kasthuriengan S (2012) Influence of stack geometry and resonator length on the performance of thermoacoustic engine. *Appl Acoust* 73:1052–1058
25. Swift GW (2002) Thermoacoustics: a unifying perspective for some engines and refrigerators. *Acoust Soc Am* 113:1–4
26. Atchley AA, Bass HE, Hofler TJ, Hsiao-Tseng L (1992) Study of a thermoacoustic prime mover below onset of self-oscillation. *J Acoust Soc Am* 91(2):734–743
27. Lamb H (1932) *Hydrodynamics*, 6th edn. Cambridge University Press, Cambridge
28. Arnott WP, Bass HE, Raspet R (1991) General formulation of thermoacoustics for stacks having arbitrarily shaped pore cross sections. *J Acoust Soc Am* 90(6):3228–3237
29. Swift GW, Keolian RM (1993) Thermoacoustics in pin-array stacks. *J Acoust Soc Am* 94(2):941–943
30. Song L, Koopmann GH, Hoffmann TL (1994) An improved theoretical model of acoustic agglomeration. *J Vib Acoust Trans ASME* 116(2):208–214
31. Arnott WP, Belcher JR, Raspet R, Bass HE (1994) Stability analysis of a helium-filled thermoacoustic engine. *J Acoust Soc Am* 96(1):370–375
32. Rott N (1980) Thermoacoustics. *Advances in applied mechanics*. Academic Press, London, pp 135–175
33. Ueda Y, Kato C (2008) Stability analysis of thermally induced spontaneous gas oscillations in straight and looped tubes. *J Acoust Soc Am* 124(2):851–858